Materials Science-Poland
Volume 42 Issue 4 · pp. 163–179 · DOI: 10.2478/msp-2024-0051

sciendo

Materials Science-Poland

Evaluation of microstructural and mechanical qualities in optimised TIG-welded SDSS 2507 joints

Research Article

Sujeet Kumar[1]*, Madugula Naveen Srinivas[1], Naveen Kumar[2], Jayant Giri[3,4,5], Amanullah Fatehmulla[6], Saurav Mallik[7]

[1] Department of Mechanical Engineering, Bonam Venkata Chalamayya Engineering College, Odalarevu, 533210, East Godavari, Andhra Pradesh, India
[2] Department of Mechanical Engineering, United College of Engineering and Research, Naini, Prayagraj, Uttar Pradesh, 211010, India
[3] Department of Mechanical Engineering, Yeshwantrao Chavan College of Engineering, Nagpur, India
[4] Division of Research and Development, Lovely Professional University, Phagwara, India
[5] Centre for Research Impact & Outcome, Chitkara University Institute of Engineering and Technology, Chitkara University, Rajpura, 140401, Punjab, India
[6] Department of Physics and Astronomy, College of Science, King Saud University, Riyadh, 11451, Saudi Arabia
[7] Department of Environmental Health, Harvard T H Chan School of Public Health, Boston, MA, United States of America

Received 29 November 2024; Accepted 13 January 2025

Abstract: Super duplex stainless steel (SDSS) is gaining attraction owing to its excellent mechanical strength and superior corrosion resistance. In this study, tungsten inert gas (TIG) was implemented for welding the SDSS thin sheet. The Taguchi method and analysis of variance (ANOVA) were carried out by selecting L_{25} orthogonal arrays. The optimum TIG parameters were a welding current of 75 A, an arc potential of 15 V, a welding rate of 120 mm/min, and an argon gas consumption rate of 12 L/min. An ANOVA study found that welding current (46.95%) was the largest contributor in producing the excellent welded joint. The microstructural research indicated increased grain size in the heat-affected zone (HAZ) and fusion zone (FZ), represented by distinct grain boundary layers, intragranulars, and Widmanstätten austenite. This was due to heat input and rapid cooling inclusion as well as re-crystallisation of the ferrite matrix. The elemental mapping analysis showed that chromium must be present to generate a shielding oxide layer, which decreased from 25.50% in the parent material to 23.40% in the TIG welded joint. The tensile test found that TIG welds had an ultimate tensile strength (UTS) of 789 MPa. This value was equivalent to the base metal UTS value of 800 MPa. The micro-hardness test of the TIG welded joint confirmed that the HAZ (350 HV) and FZ (325 HV) were higher than that of the base metal (305 HV). The hardness value near the FZ boundary experienced a significant increase due to the development of hard microscopic components and element migration during the TIG process.

Keywords: *Tungsten inert gas • Super duplex stainless steel • Elemental mapping • Microstructure • Tensile test • Microhardness*

1. Introduction

Super duplex stainless steel (SDSS) is a standard alloy with a unique dual-phase microstructure made up of γ-austenite and α-ferrite phases in equal quantities [1–4]. Due to its dual microstructure, SDSS has outstanding mechanical properties and excellent resistance to corrosion [5–7]. The pitting resistance equivalent number (PREN) for the SDSS is 42 (Cr% + 3.3 × Mo% + 16 × N%). The alloy has a PREN grade above 40, which is highly resistant to pitting corrosion [8,9]. The outstanding qualities of SDSS make it the chosen material for tough working conditions in numerous sectors, such as the oil and gas, petrochemical, chemical processing, and maritime operations [10,11]. These industries utilise SDSS products in severe corrosion as well as mechanical strain [12–14].

Welding is an essential joining process to utilise in the implementation of SDSS material for various applications [15,16]. The heat input and rate of cooling are crucial elements that can determine the austenite–ferrite proportion and the production of additional phases while welding. The equilibrium of austenite and ferrite phases is critical for optimum mechanical strength and resistance to corrosion [7,17]. The brittleness is caused by an increased ferrite

---

* *E-mail: sujeet731@gmail.com*

concentration within the area of fusion zone (FZ), while corrosion resistance declines with a greater austenite content. In addition to phase balance, the main issue is the development of harmful phases during the welding process, including sigma (σ), chi (χ), and nitrides. It decreases the welded joint's mechanical qualities and resistance against corrosion [18,19]. To get the maximum mechanical strength and resistance against corrosion, adopting the best welding process and filler substance is essential. In order to achieve this equilibrium and maintain an optimal austenite amount that enhances mechanical capabilities, austenitic filler metals are frequently utilised in arc welding processes [14,20]. Hot cracking during the process of welding is a significant challenge when welding the SDSS material. This can be reduced using a filler metal together with a ferrite stabiliser [21,22].

Tungsten inert gas (TIG) is widely utilised for welding SDSS. The method is appreciated for its excellent accuracy and capacity to generate superior welds with minimal defects [23–25]. Ramkumar et al. [26] concentrated on optimising the TIG welding parameters for thick sheets of SDSS to enhance welds' mechanical qualities. Their efforts produced exceptional results, achieving an elastic strength equal to 851 MPa with an impact toughness around 150 J in the TIG welding joints. Vahman et al. [27] discovered that increasing the thermal input ranges 1.19–1.87 kJ/mm diminished the ferrite content from 59 to 49%. The weld joint's microhardness was higher than the base metal's microhardness, and durability enhanced with higher temperature input [27,28]. Shin et al. [29] examined the impact of TIG welding parameters, which affected the corrosion resistance of duplex steel welds. Insufficient reheating induced by insufficient heat input during multilayer welding resulted in the formation of acicular additional austenite. The shortage of the elements chromium (Cr) and molybdenum (Mo) in ferrite inside acicular austenite reduced the PREN value, thereby reducing the corrosion resistance. Kordatos et al. [30] tested the influence of the rate of cooling on SDSS welded joints. The TIG welded joints experienced initial cooling in air, followed by immersion in cold water. Cooling with water joints exhibited enhanced hardness due to the formation of more resilient ferrite. Rapid cooling in water declined the corrosion properties, leading to diminished welding toughness. Elevated cooling rates may establish a constant austenite loop encircling ferrite grains, hence enhancing the corrosion resistance. Tavares et al. [31] found that the optimum TIG heat input for welding the SDSS material was 0.6–2 kJ/mm. For root pass welding, the heat input ranges were 1.6–2.1 kJ/mm and 1–2 kJ/mm for filler runs. Yousefieh et al. [32] employed the optimisation technique to optimise the TIG process parameters, for the maximum ultimate tensile strength (UTS) of the SDSS welds. The optimal welding parameters were established utilising 3 Hz pulse frequency, 120 A pulses of current, 60 A background current, with 40% on-time. The expected tensile test UTS of 776 MPa corresponded closely to the observed UTS, which was 769 MPa. Srirangan and Paulraj [33] used the optimisation (Taguchi) technique for optimising the welding current, arc potential across it, and speed of welding for optimum UTS and yield strength at temperatures that vary up to 750°C. The most suitable welding parameters were 110 A welding current, 12 V arc potential, and 1.5 mm/s torch speed. Magudeeswaran et al. [34] adopted the optimisation technique (Taguchi) for optimising TIG circumstances for TIG-welded SDSS joints. To produce the best weld quality, the parameters must be 140 A TIG current with a 1 mm arc width and 130 mm/min welding speed, with an operating potential of 12 V. In this study, the heat input required to weld the SDSS thin sheets using the TIG process was optimised by adjusting the weld current, arc potential, feed rate, and argon gas flow rate to attain optimum penetration. The Taguchi method was used to optimise the TIG settings, and an analysis of variance (ANOVA) study was used to determine how each parameter influenced the final results [35,36]. The SDSS thin sheet was further welded with specially modified parameters. The base metal, heat-affected zone (HAZ), and fusion zone (FZ) each undergo mechanical and metallurgical testing. A comprehensive structure–property correlation was established using optical microscopy and scanning electron microscopy (SEM) images. The findings of this study provide detailed information regarding the way welding parameters influence the metallurgy and mechanical features of SDSS joints.

2. Materials and testing processes

2.1 Materials and welding process

The current research utilised a thin sheet of SDSS 2507, with the dimensions of SDSS base metal being 150 mm × 100 mm × 2 mm. The chemical composition of SDSS is presented in Table 1 and the mechanical properties of SDSS 2507 base metal are given in Table 2. Table 3 presents the operational range of variables for the TIG process. The flow chart representing the layout of the study is shown in Figure 1. Figure 2(a) depicts the GTAW experimental setup and Figure 2(b) and (c) shows both the top and bottom beads of an SDSS welded plate, respectively, produced using the TIG process. Prior to welding, the workpiece was cleaned with a brush made of wire. All welding

Element	Cr	Mo	Si	N	Ni	O	C	Cu	Fe
Weight (%)	25.7	3.01	0.32	0.23	7.3	0.9	0.1	0.21	Balance

Table 1. Chemical structure of SDSS.

Grade	UTS (MPa)	0.2% proof yield strength (MPa)	Minimum elongation (%)	Hardness	
				Rockwell hardness	Brinell hardness
2507	800–850	550–560	14–15	31–33	309–312

Table 2. Mechanical properties of SDSS grade 2507 [37].

S. No	TIG parameters	Range
1	Welding current intensity (A)	70–80
2	Arc potential (V)	12–16
3	Feed rate (mm/min)	80–120
4	Argon gas flow rate (L/min)	8–16

Table 3. TIG process settings.

experiments were carried out through the “FRONIUS MAGIC WAVE welder equipment” utilising 2.4 mm size non-consumable tungsten electrodes. It is an autogenous welding process, so no filler material was required. Numeric Control was used along with the welding equipment to regulate the rate of welding. Clean argon gas (99.99%) was employed for welding to improve the arc consistency and prevent the pool of welding fluid against environmental contaminants (such as oxidation). Equation (1) was used to calculate the heat input (Q) of the TIG process.

$$Q = (\eta \times I \times V)/S, \tag{1}$$

where Q represents the heat input (J/mm), I is the welding current (A), η is the welding efficiency, V is the arc potential, and S is the welding rate (mm/s).

2.2 Microstructural characterisation method

Microstructural examination of SDSS base metal and welded joints was carried out. The samples were consistently abraded using silicon carbide emery papers with a precision of up to 2,000. Abrasion eliminates all surface defects, producing an even as well as equal finish. After abrasion, the specimens were then polished with alumina powder and diamond paste (1 µm) to achieve a mirror

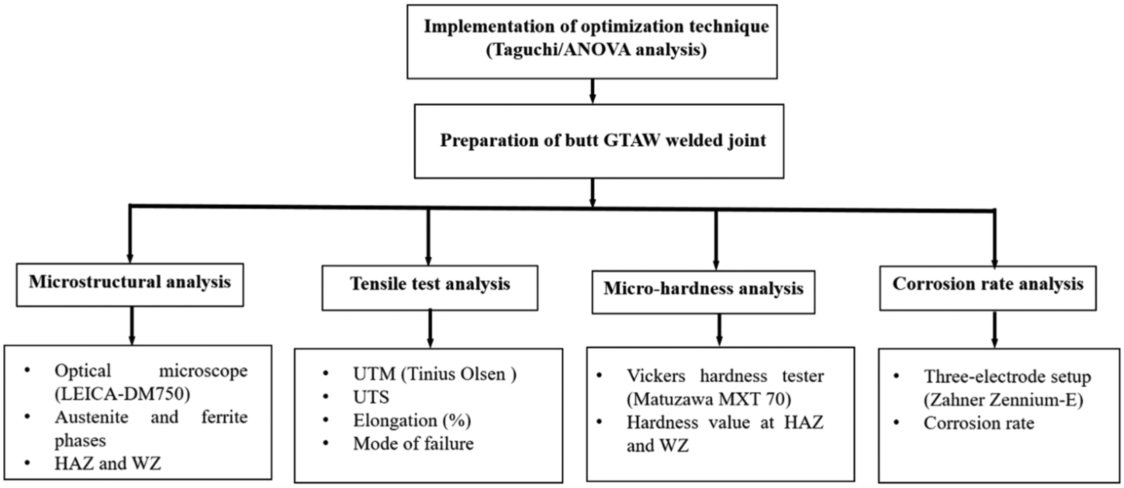

Figure 1. Layout of the research.

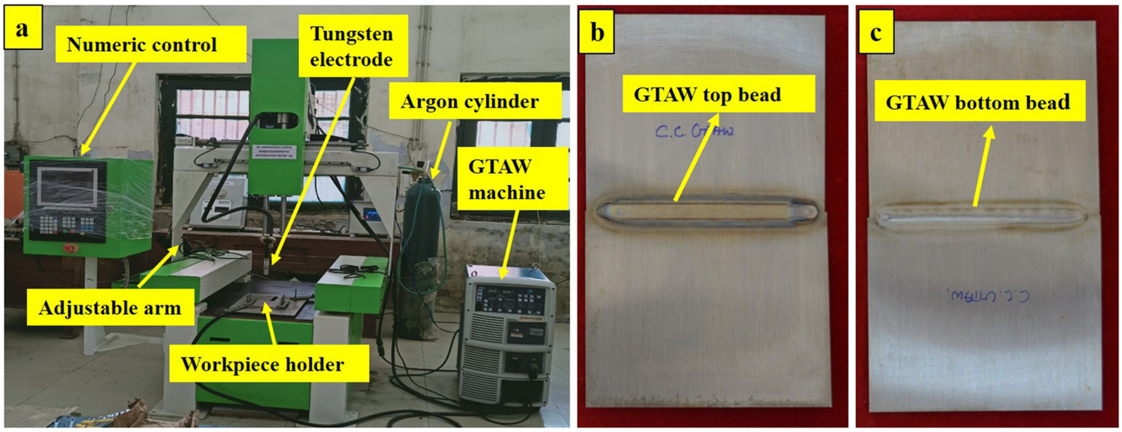

Figure 2. (a) TIG experimental setup. SDSS plate welded by the TIG process: (b) top bead and (c) bottom bead.

finish. Following polishing the specimens to the desired level of softness, they were etched to reveal the internal microstructure [38]. The etching method used Kalling's solution, which is a mixture of 100 mL of ethanol, 5 g copper chloride ($CuCl_2$), and 100 mL of hydrochloric acid. The samples were carefully immersed in the etching solution, which targeted the grain boundaries. Finally, the etched samples were analysed under an optical microscope (LEICA-DM750) to determine their microstructures, which included grain size, phase distribution, and any possible defects. The elemental analysis of the SDSS base metal with TIG welded joints was carried out by energy-dispersive X-ray spectroscopy (EDX) using a ZEISS EVO MA15 scanning electron microscope coupled with an EDX sensor. The scanning electron microscope was operated in high-vacuum mode at a voltage gradient of 20 kV, which was tuned towards effective X-ray production and elemental analysis.

2.3 Mechanical property tests

Mechanical tests were carried out for SDSS base metal as well as TIG welded joints. The tensile test was conducted with a universal testing machine (UTM) (Tinius Olsen) at a strain rate of 1 mm/min, which is illustrated in Figure 3(a), and the tensile test sample before fracture is shown in

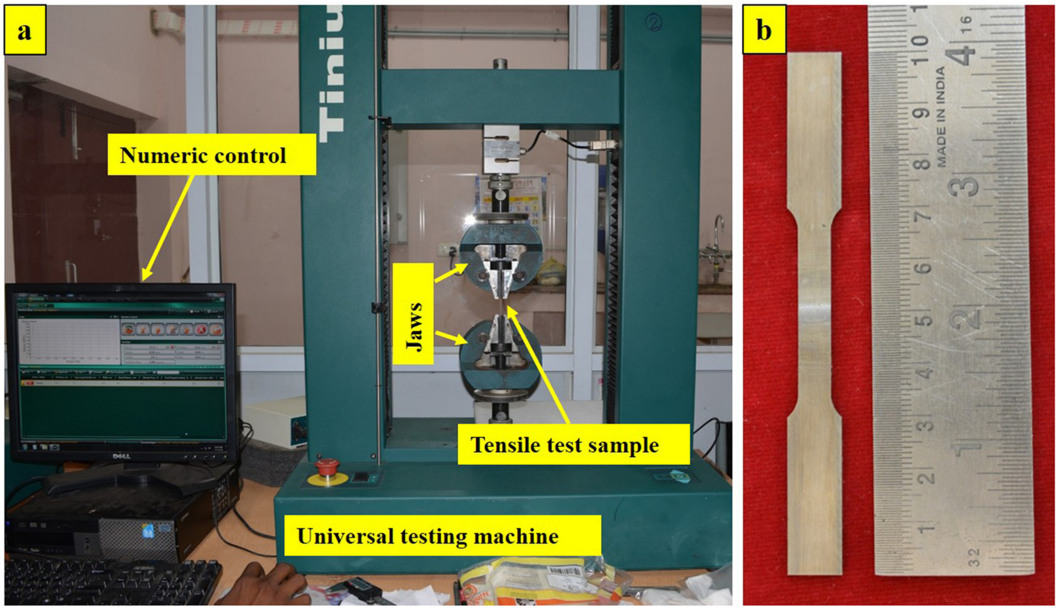

Figure 3. (a) UTM for tensile tests and (b) tensile test sample before fracture.

Figure 3(b). The test specimens were developed in line with the requirements of the ASTM E8/E8M to assure excellent dimension conformity [39]. The specimens were set in the UTM and produced a uniaxial tensile force till fracture. Data were obtained to create stress–strain graphs for yield strength, tensile strength, and elongation. The broken tensile test specimens were evaluated with the help of a Hitachi S-3000N scanning electron microscope for analysing the tensile test fracture surfaces and establishing the failure mode, offering details about the material's mechanical behaviour and the quality of the weld. The microhardness of FZ and HAZ was determined using a Vickers hardness tester; the testing began in the middle of the metal that is being welded and moved on to the base metal through HAZ. Three independent locations were determined at every stage of every test area using a 500 g load with 10 s of dwell time. The final outcome was determined from the average of multiple readings to provide accurate and reliable data. For each characterisation, three samples were tested for getting consistent results.

3. Optimisation techniques

3.1 Taguchi method

The Taguchi method is a commonly used optimization technique that improves the efficiency and performance of structures, processes, and products by reducing trial duration and expenses. It optimises the response by fitting an equation with polynomials to the experimental data, and it is ideal for modelling and analysing issues with several variables influencing the outcome. This strategy employs carefully planned trials to discover the optimal conditions by calculating the impact of TIG parameters and the way these interact with each other. The methodology employs ANOVA to get the most essential parameter. It also entails building response interfaces to understand whether the factors influence the response. Using Taguchi, this research determined the optimal process parameters by altering four variables that significantly affect the caliber of the weld durability [40]. The TIG parameters used include the welding current, arc potential, feed rate, and argon gas flow. The experiments were designed with a fundamental compound structure to provide reliable and durable outcomes, and the experimental layout was carefully developed.

3.2 ANOVA

ANOVA was employed to make a prediction regarding the relevance of the TIG parameters. It is useful for finding out whether various parameters affect the output variable. It analyses mean squares with error from experiment predictions across different confidence levels to identify the value of the major components and their interactions. This study analyses the peak strength of the welded joints on tensile strength, elongation (%), and micro-hardness. Table 4 lists the TIG process parameters utilised in the bead on plates' TIG process. The property of a matrix that contrasts the mean to variance with the optimal value is the *S*/*N* ratio. Equations (2)–(4) can be utilised to calculate the signal-to-noise (*S*/*N*) ratio. By assessing the mean and *S*/*N* ratio utilising the output variables – tensile strength, elongation (%), and microhardness – it is possible to ascertain the optimal joint integrity as well as the TIG process parameters that affect the welded joints' quality. The mean and *S*/*N* ratio were calculated to assess whether each process factor affects the joints that are welded. Utilising the nominal is better (micro-hardness) and larger the better (tensile strength elongation) standards, the mean and *S*/*N* ratio were selected in this study to ascertain the response of the process parameters. These variables determine the joint strength of the welded component, and they were evaluated using MINITAB software.

Nominal is best for microhardness [41]:

$$\frac{S}{N}\text{ratio} = -10\log 10\left(\frac{1}{n}\right)\sum_{b=1}^{n}(yb - y')^2. \tag{2}$$

Larger the better for tensile test (UTS, elongation) [41]:

$$\frac{S}{N}\text{ratio} = -10\log 10\left(\frac{1}{n}\right)\sum_{b=1}^{n}\frac{1}{yb^2}. \tag{3}$$

Smaller the better for corrosion rate and power consumption [41]:

TIG parameters	Unit	Level				
		1	2	3	4	5
Welding current	A	70	72	75	77	80
Arc potential	V	12	13	14	15	16
Feed rate	mm/min	80	90	100	110	120
Argon gas flow rate	L/mm	8	10	12	14	16

Table 4. Process parameters for the TIG bead on plate.

$$\frac{S}{N}\text{ratio} = -10\log 10\left(\frac{1}{n}\right)\sum_{b=1}^{n} yb^2, \tag{4}$$

where n is the total amount of measurements, yb is the obtained data, and y' is the mean of the previously obtained experimental data.

4. Results and discussion

4.1 Taguchi outcome analysis

The butt joints of the SDSS (thin) material sheet were produced by changing the welding process parameters, including the welding current, arc potential, feed rate, and argon gas flow rate. Table 5 provides the values of all input parameters and responses (UTS, elongation [%], and microhardness).

4.2 *S/N* ratio analysis

Tables 6–8 present the response data for *S*/*N* ratios (bigger is better) of UTS and elongation (%), as well as the response chart for *S*/*N* ratios (smaller is better) of micro-hardness. The effect of welding current greatly impacts micro-hardness, suggesting that welding current is a predominant factor making the welded joints. The elevated cooling rate at increased thermal energy input may be the root cause of this occurrence. The elevated cooling rate

Experiment	Factors				Outputs			
	Welding current (A)	Arc potential (V)	Feed rate (mm/min)	Argon gas flow rate (LPM)	UTS (MPa)	Elongation (%)	Hardness (HV)	Heat input (kJ/mm)
1	70	12	80	8	754	22.7	330	0.567
2	70	13	90	10	753	22.6	331	0.546
3	70	14	100	12	752	23.4	332	0.529
4	70	15	110	14	751	22.2	332	0.515
5	70	16	120	16	755	21.5	334	0.504
6	72	12	90	12	755	22.5	335	0.518
7	72	13	100	14	756	21.8	334	0.505
8	72	14	110	16	751	22.6	335	0.495
9	72	15	120	8	754	29.7	336	0.486
10	72	16	80	10	752	21.2	337	0.778
11	75	12	90	16	755	21.3	323	0.540
12	75	13	100	8	756	23.9	331	0.527
13	75	14	110	10	754	22.8	332	0.515
14	***75***	***15***	***120***	***12***	***789***	***24.7***	***325***	***0.506***
15	75	16	90	14	763	25.7	322	0.720
16	77	12	110	10	761	24.4	324	0.454
17	77	13	120	12	758	23.2	340	0.450
18	77	14	80	14	759	23.6	340	0.728
19	77	15	90	16	763	25.6	324	0.693
20	77	16	100	8	757	23.8	326	0.665
21	80	12	110	14	758	22.2	327	0.471
22	80	13	120	16	765	23.7	338	0.468
23	80	14	90	8	762	23.4	326	0.672
24	80	15	100	10	768	23.6	327	0.648
25	80	16	110	12	758	23.8	328	0.628

Table 5. L_{25} array for TIG parameters and their corresponding output. Italic and bold text shows optimized parameters of welded joint.

Level	Welding current (A)	Arc potential (V)	Feed rate (mm/min)	Argon gas flow rate (L/min)
1	57.51	57.57	57.56	57.57
2	57.54	57.57	57.59	57.57
3	57.60	57.56	57.56	57.59
4	57.60	57.59	57.56	57.57
5	57.61	57.58	57.59	57.57
Delta	0.10	0.04	0.03	0.02
Rank	1	2	3	4

Table 6. Response table for *S*/*N* ratios for UTS (larger is better).

resulted in a finer grain structure, hence improving the mechanical characteristics of the welds, such as UTS and elongation (%). Therefore, enhanced weld reinforcing was achieved by increased weld penetration at lower feed rates and elevated welding current. Consequently, higher welding currents led to increased UTS and elongation. ANOVA was conducted using Minitab software at 95% confidence level ($\alpha = 0.05$) to identify the significant controllable factor and its corresponding contribution to the response variables. The optimal settings were a welding current of 75 A, an arc potential of 15 V, a feed rate of 120 mm/min, and an argon gas flow rate of 12 L/min. ANOVA findings are provided in Table 9, showing that welding current contributes the most at 46.95%, followed by argon gas flow rate at 24.56%, feed rate at 13.26%, and arc potential at 10.25%. Figure 4(a)–(c) shows the impact of each parameter on UTS, elongation, and microhardness, respectively.

4.3 Development of a mathematical model for regression analysis

The formula for regression correlates the input values of process variables (welding current, arc potential, feed rate, and argon gas flow rate) with the response outcomes (UTS, elongation, and microhardness). The results of this research used Taguchi's L25 orthogonal arrays; a total of 625 trials and 25 experiments have been conducted. The objective of regression modelling in the present investigation is to determine the responses for middle tests that exclude welded joints. Regression equations are presented in equations (5)–(7).

Level	Welding current (A)	Arc potential (V)	Feed rate (mm/min)	Argon gas flow rate (L/min)
1	26.60	27.00	26.91	26.97
2	26.80	27.04	27.21	27.03
3	27.32	26.91	26.95	27.25
4	27.28	27.26	26.96	27.07
5	27.35	27.14	27.25	27.03
Delta	0.75	0.35	0.34	0.29
Rank	1	2	3	4

Table 7. Response table for *S*/*N* ratios for elongation (%) (larger is better).

$$\begin{aligned}\text{UTS} = {} & 0.24445 + 1.24153 \text{ welding current} - (-0.3524622) \\ & \text{arc potential} + 4.132543 \text{ feed rate} \\ & + 0.01564 \text{ Argon gas flow,}\end{aligned} \tag{5}$$

$$\begin{aligned}\text{Elongation} = {} & 3.11 - 0.35245 \text{ welding current} \\ & + 1.7845 \text{ arc potential} \\ & + 4.32625 \text{ welding speed} \\ & + 0.035264 \text{ Argon gas flow,}\end{aligned} \tag{6}$$

$$\begin{aligned}\text{Hardness} = {} & -19.3275 + 1.39285 \text{ welding current} \\ & - 0.625684 \text{ arc potential} \\ & + 5.05 \text{ welding speed} \\ & + 0.31254 \text{ Argon gas flow.}\end{aligned} \tag{7}$$

4.4 Confirmation tests

The confirmatory test was performed at appropriate circumstances to check the welded joint's characteristics of quality. Optimal conditions for the confirmation test were 75 A welding current, 15 V arc potential, 120 mm/min feed rate, and 12 L/min argon gas flow rate. The optimised parameters produced an UTS of 789 MPa, an elongation of 24.7%, and a hardness of 325 BHN. The next sections

Level	Welding current (A)	Arc potential (V)	Feed rate (mm/min)	Argon gas flow rate (L/min)
1	−48.86	−48.95	−48.95	−48.96
2	−48.87	−48.93	−48.92	−48.97
3	−48.95	−48.96	−48.96	−48.95
4	−49.01	−48.94	−48.96	−48.93
5	−49.00	−48.92	−48.93	−48.90
Delta	0.15	0.04	0.04	0.07
Rank	1	3	4	2

Table 8. Response table for *S*/*N* ratios for micro-hardness (smaller is better).

Source	DF	Adj SS	Adj MS	*F*-value	*P*-value	Contribution (%)
Welding current	4	309.75	77.436	6.12	0.015	46.95
Arc potential	4	18.43	4.607	0.36	0.828	10.25
Feed rate	4	41.63	10.406	0.82	0.546	13.26
Argon gas flow rate	4	18.52	4.631	0.37	0.826	24.56
Error	8	101.15	12.644			4.98
Total	24	490.26				

Table 9. Results of ANOVA.

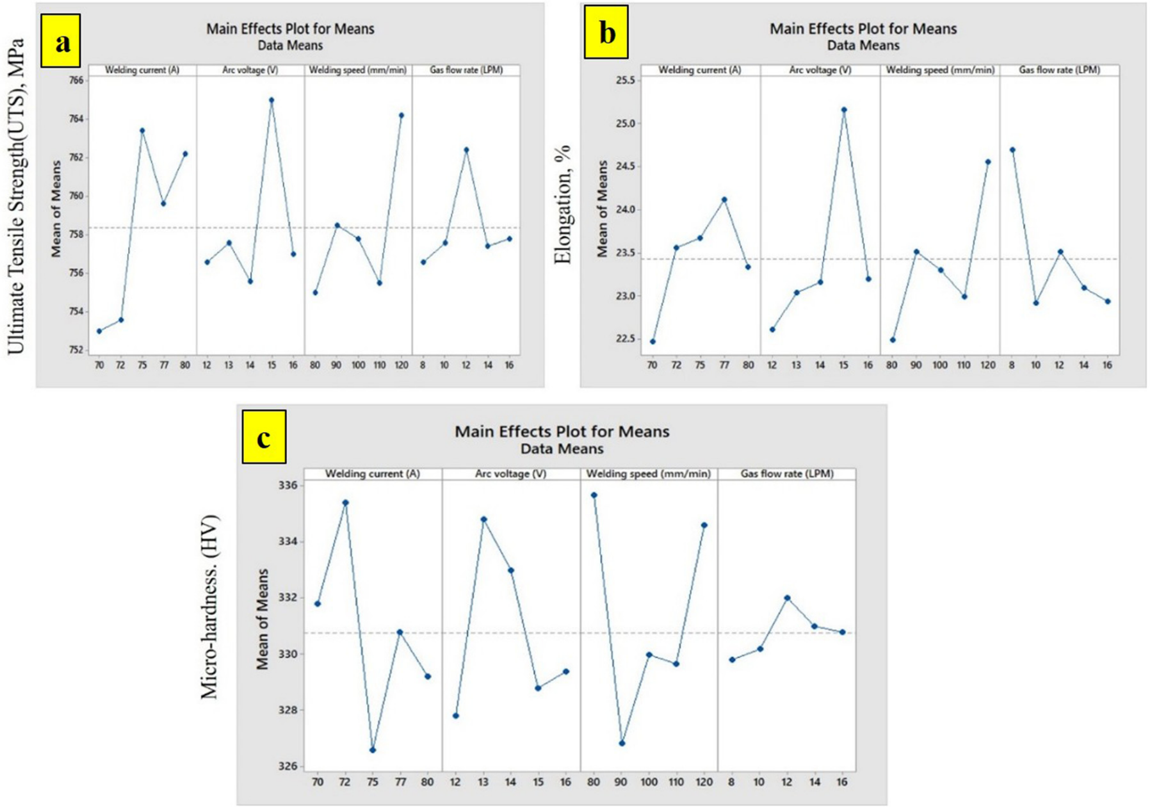

Figure 4. Contribution of each parameter: (a) UTS, (b) elongation, and (c) microhardness.

provide a detailed investigation of microstructural analysis, UTS, % of elongation, and microhardness analysis.

4.5 Microstructural analysis

The macrostructures of the weld top and root regions are shown in Figure 5. In the welding operation, the weld root sections were melted. The increased grain size absorption occurred within the HAZ and FZ, as shown in Figure 6(a) and (b). It occurs from re-crystallisation of the ferrite framework and participation of heat input and cooling rates. Consequently, acicular secondary austenite develops at the root, while main austenite develops inside the grains. In contrast to the weld top region, the root region produces higher austenite. Three forms of austenite, that is, grain boundary, intra-granular, and Widmänstten austenite occur inside a ferrite matrix which makes up the weld top area, as shown in Figure 6(c). The higher heat input (≥0.778 kJ/mm) produced bigger grains, greater austenite proportion, and slower cooling rate in SDSS welds. The finer grains, less austenite concentration, and more rapid cooling had been

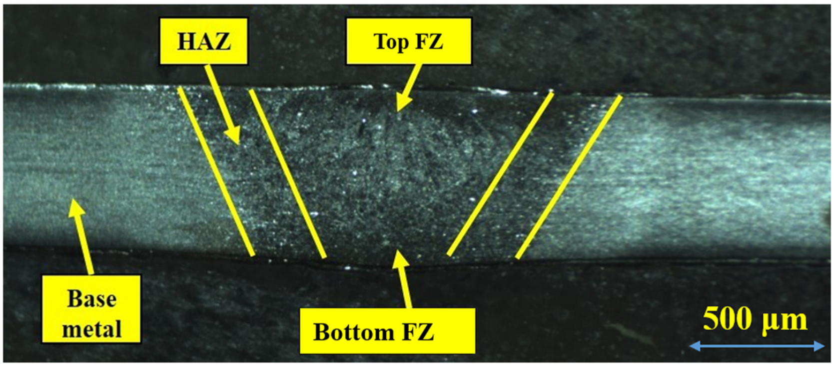

Figure 5. Macrostructure of the TIG welded joint of the SDSS sheet.

the outcomes of the reduced heat input (<0.778 kJ/mm) in SDSS welds. Austenite was produced here within and between grains. Table 10 presents the ferrite level present in the welded joints. In the FZ and the HAZ, a higher ferrite content was noted in the weld top compared to the root region. It is evident that the amount of ferrite volume percentage in the HAZ exceeds that of the FZ. One austenitic stabiliser was nitrogen. The ferrite content of the FZ and HAZ welded by the TIG process was reduced by the addition of nitrogen content (Ar + 2% N). The right austenite–ferrite ratio was

Heat input (kJ/mm)	Top weld	Root weld	Top HAZ	Root HAZ
0.546	66	33	62	58
0.486	57	30	59	57
0.506	50	27	58	55
0.495	48	26	55	52

Table 10. Ferrite percentage of SDSS in the FZ and HAZ with varying heat input.

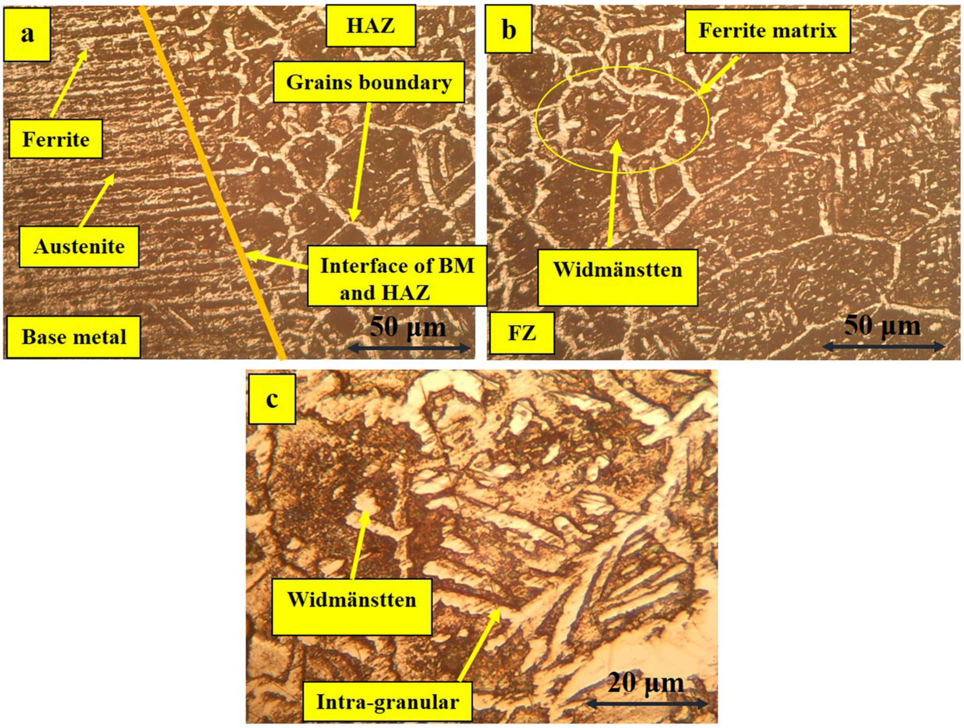

Figure 6. Microstructure of (a) base metal and HAZ, (b) FZ, and (c) enlarged view of FZ.

obtained, and improved mechanical characteristics were enhanced by increasing the nitrogen content from 2 to 5%. In comparison to 5% nitrogen, 2% nitrogen is more affordable and readily available on the market while still providing the required phase stability. Consequently, based on the results, a gas with 2% nitrogen is adequate to support the equilibrium state.

4.6 SEM and elemental mapping analysis

The SEM micrograph of the TIG-welded component of the SDSS shows a microstructure that is highly characterised. The base metal SEM image shown in Figure 7(a) reveals elongated, acicular ferrite, and austenite phases spread out in the matrix. The welded joint's SEM study shows clear phase boundaries and areas with needle-like structures related to the Widmanstätten austenite formed during the welding process, as shown in Figure 7(b). The ferrite phase is converted to long grains of Widmanstätten austenite, as indicated in Figure 7(c); the results show that mechanical strength is increased and the margin is decreased in corrosion resistance. Ferrite is resistant to rust, and austenite makes things tougher. The comparative EDX analysis of the SDSS base metal and SDSS welded joint shows slight but substantial elemental composition changes due to TIG welding. Chromium (Cr) must be present to generate the shielding oxide layer, which decreases from 25.50% in the base metal to 23.40% in the welded joint. Nickel (Ni) increases the toughness and ductility, and the austenite phase may become unstable as its Ni percentage decreases from 6.80 to 5.10%. The content of manganese (Mn) increases from 2.47% in the base metal to 3.72% in the weld due to the thermal cycle that assists diffusion, as shown in Figure 8. Mn is a deoxidiser and stabilises weld pools and FZ. The element molybdenum (Mo) improves the welded area pitting resistance by increasing it from 1.55 to 1.59%, which is beneficial in chloride-rich situations. Silicon

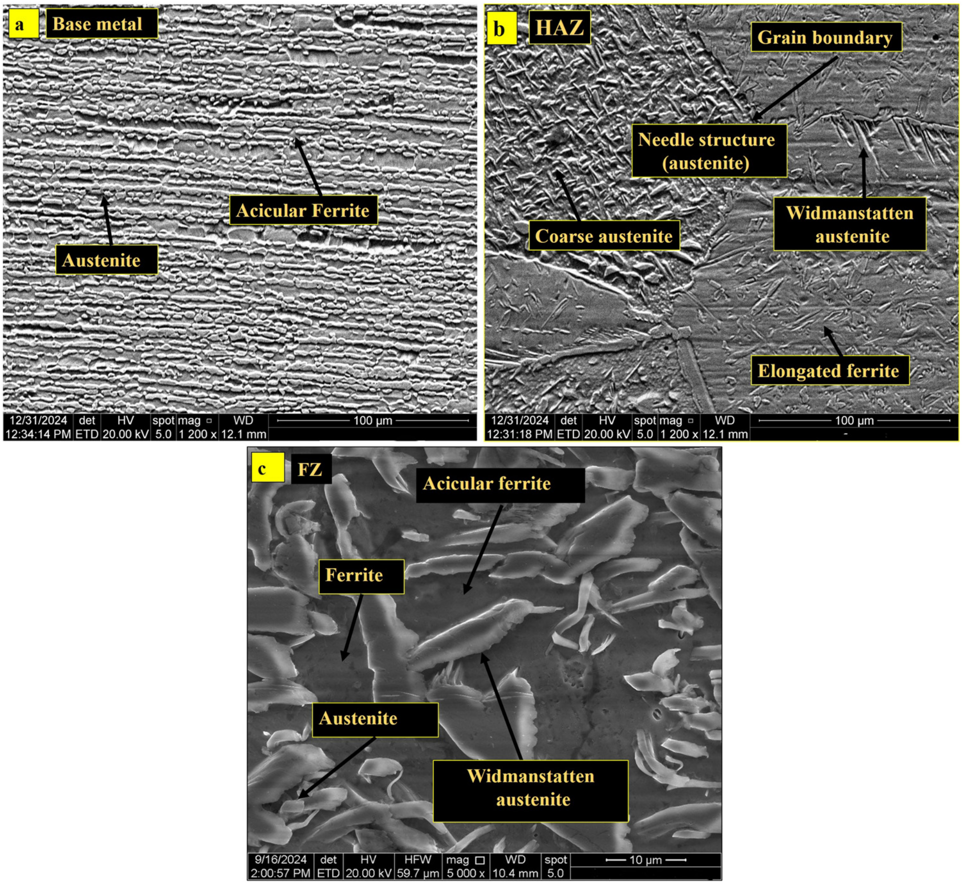

Figure 7. SEM images of (a) base metal and of welded joint's (b) HAZ and (c) FZ.

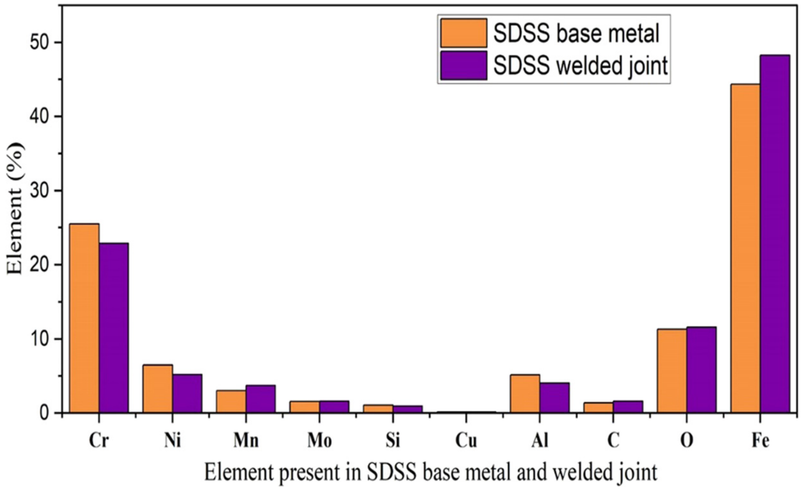

Figure 8. Elemental mapping of the base metal and welded joint.

(Si) decreases from 1.06 to 0.93%, possibly owing to welding intake decreasing the oxidation resistance.

4.7 Tensile test analysis and fracture analysis

Figure 9(a) presents the fractured tensile test sample of base metal, while Figure 9(b) shows the enlarged view of broken tensile test samples. Figure 9(c) shows the welded tensile test fractured sample, and Figure 9(d) shows the enlarged view of broken welded tensile test samples. The fact that the HAZ represents the weak portion of welds. The UTS of TIG welded joint's is 789 MPa, as observed by the tensile test. According to the stress–strain curves in Figure 10, the UTS of the base metal typically ranges from 730 to 800 MPa, which is slightly higher than the welded joint. The TIG process lowers the tensile strength

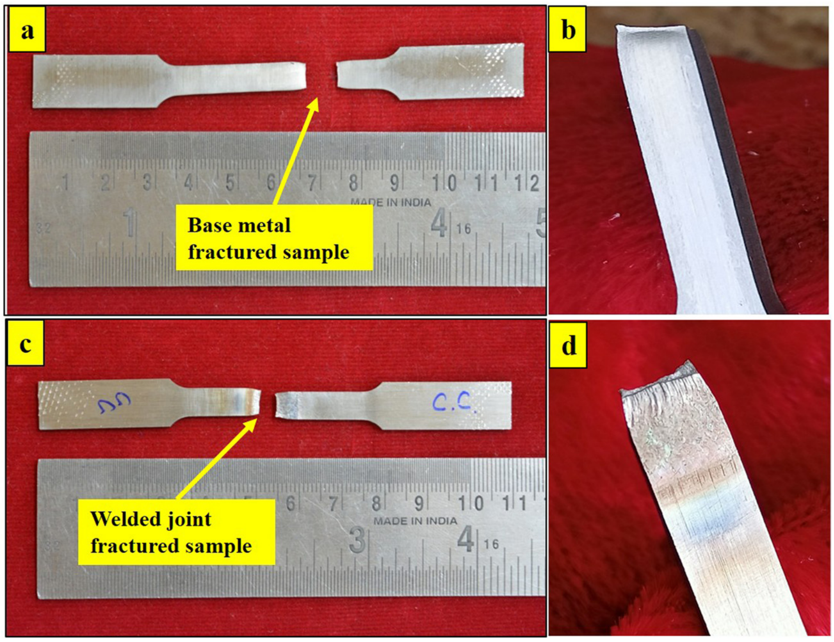

Figure 9. Tensile test samples: (a) base metal, (b) broken base metal, (c) TIG welded, and (d) broken TIG welded joint.

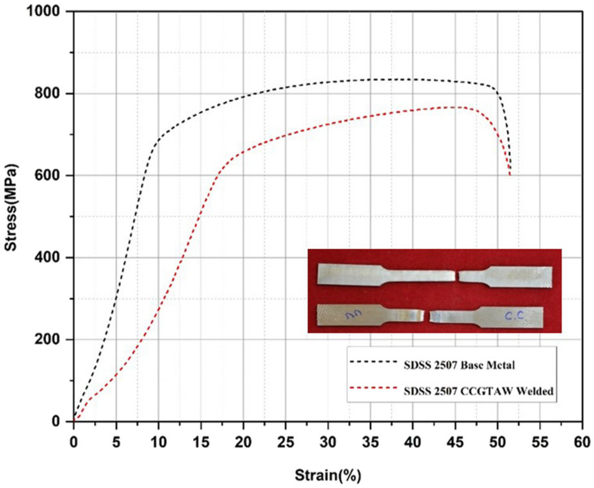

Figure 10. Stress–strain diagram for the SDSS base metal and welded joint tensile test sample.

through the application of heat input, potentially resulting in microstructural changes, such as coarse grain formation and phase imbalance inside the FZ. The yield strength of the welds is 550 MPa, rendering it consistent with SDSS. The yield strength of the welded joint matches up with that of the base metal, indicating the effectiveness of the TIG process in keeping the material's mechanical strength. The elongation of the welded joint was recorded at 20%, coming within the usual limit for SDSS. The elongation % indicates that the welded connection has sufficient ductility, making it appropriate for applications requiring some degree of deformation under load. The retention of high yield strength and good elongation suggest that the welding process was well-controlled, with no negative

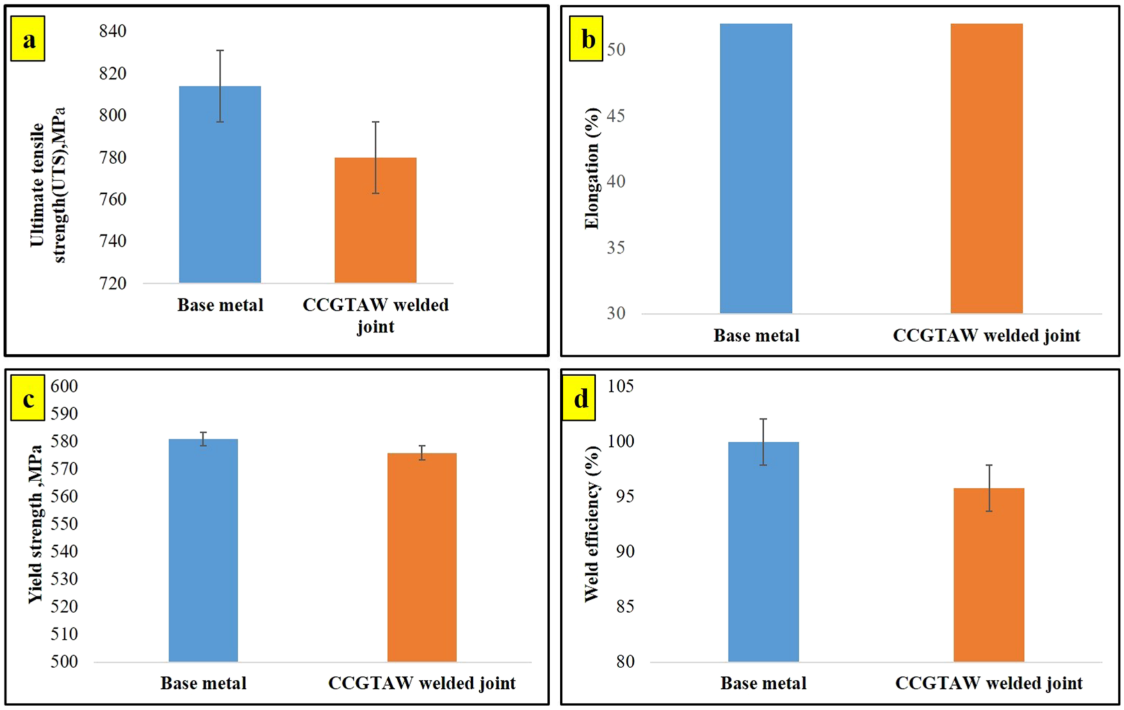

Figure 11. Bar graph of comparative study of base metal's and welded joint's (a) UTS, (b) elongation, (c) yield strength, and (d) weld efficiency.

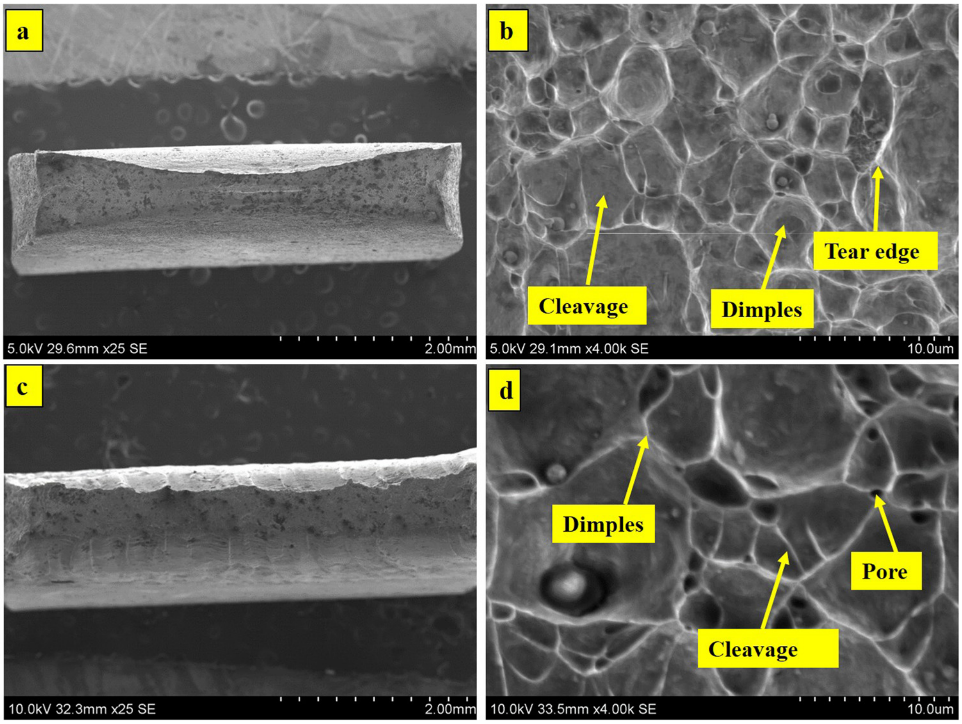

Figure 12. Fracture surfaces for the tensile test specimens with the (a) base metal, (b) a close-up view of the base metal fracture surface, (c) welded joint, and (d) a close-up view of the welded joint fracture surface.

effects on the material's mechanical properties. The Joint efficiency [$(\text{UTS}_{\text{welds}})/(\text{UTS}_{\text{base metal}}) \times 100$] achieved for the TIG process was 95.8%. The comparative study of the base metal and welded joint's UTS, elongation (%), yield strength, and weld efficiency are shown in Figure 11(a)–(d), respectively. The findings of Figure 11(a)–(d) indicate that while tensile and yield strength are slightly lower in the weld than in the base metal, elongation remains similar. Weld efficiency surpasses 95%, indicating satisfactory mechanical reliability. Error bars show variation in data across many samples.

4.8 SEM fractography

Figure 12(a) and (c) depicts SEM images of the base metals and the fractured samples from the welded tensile test, respectively. Fracture samples usually have a fibrous

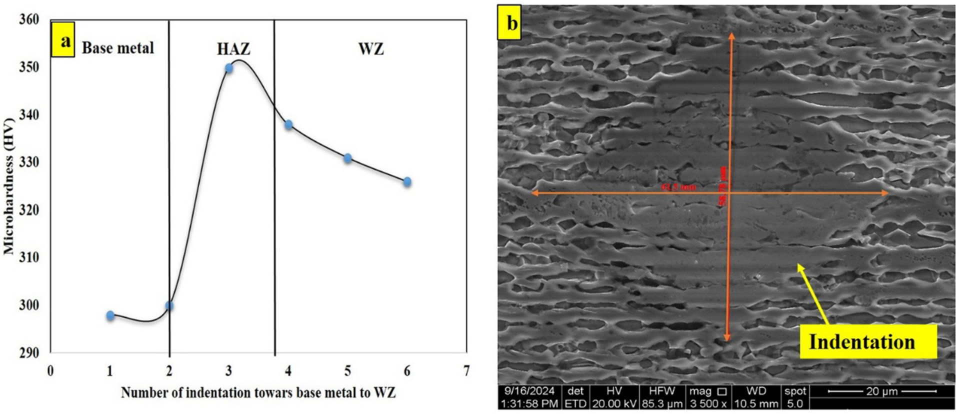

Figure 13. Micro-hardness values in the (a) base metal, HAZ, and FZ and (b) SEM image of indentation on the base metal.

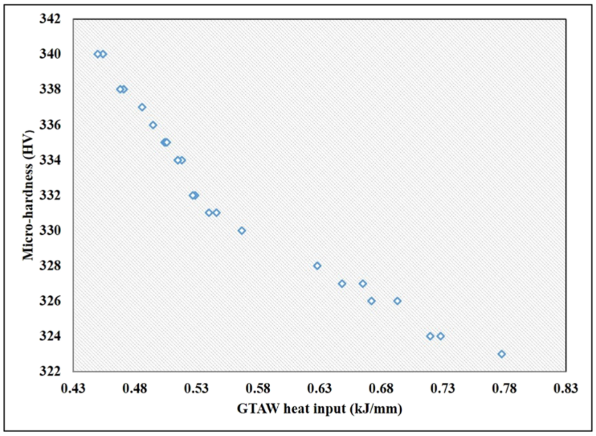

Figure 14. Micro-hardness variation with heat input.

and coarse surface marked by numerous small dimples, as illustrated in Figure 12(b) and (d). The formation of these dimples results from nucleation, and the growth and coalescence of tiny voids occur during substantial plastic deformation before fracture. A ductile fracture surface indicates that the material or weld may absorb considerable energy prior to failure.

4.9 Micro-hardness analysis

Figure 13(a) depicts micro-hardness distribution patterns at the junction between joints of the SDSS base metal, HAZ, and FZ. The micro-hardness distribution patterns over the joint interface show that the harness values of the HAZ and FZ of the welded joint exceed that of the base metal. In addition, the hardness value near the FZ boundary increases as a result of growth of hard elements and elemental shift during the TIG process. The fine equiaxed dendritic morphology and enhanced concentration of Ni and Cr in the composition are thought to be responsible for the FZ elevated hardness value. In addition to Cr, Ni, Mo, and Fe components, the fluctuation in the amount of carbon in SDSS welded joints is the key factor contributing to the greatest hardness values in the HAZ and FZ. The HAZ values are around 330 HV, higher than that of the welded joint, in accordance with the observed results in the literature [1]. The SEM image of the indented part is shown in Figure 13(b). The increased inter-pass temperatures increased the hardness values of the FZ and HAZ. One possible reason for this phenomenon is that greater inter-pass temperatures can cause the development of hard and unstable intermetallic phases as a result of slow cooling. Figure 14 shows that as the TIG heat input increases, the welded joint toughness drops. The toughness of the welded joint decreases as the TIG heat input increases. The phase transition and cooling rate variations cause hardness to decrease as the heat input increases. A decrease in hardness is produced by an increase in austenite production, and it occurs when the cooling rate slows due to increased heat input. This results in a drop in ferrite content in the welded joint. The cooling rate is much higher at low heat input because the ferrite–austenite transition is slower than at a high heat input.

5. Conclusions

In this study, TIG parameters for welding SDSS were optimised with the goal of producing a superior microstructure and improved mechanical characteristics. Butt joints from the SDSS sheet were formed by modifying TIG process parameters like welding current, arc potential, feed rate, and argon gas flow rate. To optimise the parameters, the Taguchi technique (L_{25} orthogonal array) configuration was used, and Minitab software was utilised for ANOVA.

- The welding current, arc potential, feed rate, and argon gas flow rate of 75 A, 15 V, 120 mm/min, and 12 L/min, respectively, are the ideal conditions. The outcomes of ANOVA study suggest that the highest contributors of TIG welding parameters to making the best quality TIG butt joint were welding current (46.95%), arc potential (10.25%), feed rate (13.26%), and argon gas flow rate (24.56%).

- The macrostructural study identified the HAZ and FZ in the SDSS welded joint. The microstructure of the TIG welded joint exhibited larger grain size in the HAZ and FZ. It was due to heat input and cooling rate involvement and re-crystallisation of the ferrite structure in the FZ. The austenite phase was found in the shape of the Widmanstätten structure. It was noted that the weld top had a higher ferrite content compared to the root region in both the FZ and the HAZ.

- The fracture during the tensile test took place in the HAZ, showing that it is the weakest area of the welded joint. The welded joint's UTS was found to be approximately 789 MPa. This number was slightly lower than that of the base metal's UTS, which normally varied from 730 to 800 MPa. Tensile strength was reduced due to the TIG process, which added heat and may produce microstructural changes such as grain development and phase imbalance in the FZ. The yield strength of the welded joint was measured at 550 MPa, making it compatible with SDSS 2507.

- The micro-hardness distribution patterns along the joint interaction between the base metals and FZ showed that the microhardness measurement of the HAZ (350 HV) and FZ (325 HV) of the welds exceeded that of SDSS base metal hardness (305 HV). Increased inter-pass temperature led to greater weldment hardness and HAZ values. The microhardness of the welds decreased (345 to 322 HV) when the TIG heat input increased (0.40–0.8 kJ/mm).

Acknowledgements

The authors extend their appreciation to the Researchers Supporting Project number (RSPD2025R1041), King Saud University, Riyadh, Saudi Arabia, for financial assistance.

Author contributions

Sujeet Kumar: Conceptualization, Methodology, Investigation, Writing–Original Draft, Supervision. Madugula Naveen Srinivas: Data Curation, Formal Analysis. Naveen Kumar: Experimental Work, Data Interpretation. Jayant Giri: Resources, Funding Acquisition. Amanullah Fatehmulla: Technical Guidance, Validation. Saurav Mallik: Data Analysis and validation.

Conflict of interest statement

Authors state no conflict of interest.

Data availability statement

All data that support the findings of this study are included within the article.

References

[1] Yuan, Y., Yuan, S., Wang, Y., Li, Q, Deng, Z., Xie, Y., et al., Nanostructure, mechanical properties, and corrosion resistance of super duplex stainless steel 2507 aged at 500°C, Crystals, 2023, 13: 243

[2] Köse, C., Topal, C., Dissimilar laser beam welding of AISI 2507 super duplex stainless to AISI 317L austenitic stainless steel, Mater. Sci. Eng. A, 2023, 862: 144476

[3] Wang, L., Ding, Y., Lu, Q., Guo, Z., Liu, Y., Cui, Z., Microstructure and corrosion behavior of welded joint between 2507 super duplex stainless steel and E690 low alloy steel, Corros. Commun., 2023, 11: 1–11

[4] Roos, S., Botero, C., Rännar, L.E., Electron beam powder bed fusion processing of 2507 super duplex stainless steel. as-built phase composition and microstructural properties, J. Mater. Res. Technol., 2023, 24: 6473–6483

[5] Wang, Q., Gu, G., Jia, C., Li, K., Wu, C., Investigation of microstructure evolution, mechanical and corrosion properties of SAF 2507 super duplex stainless steel joints by keyhole plasma arc welding, J. Mater. Res. Technol., 2023, 22: 355–374

[6] Sekar, C.B., Koteswara Rao, S.R., Vijayan, S., Boopathy, S.R., Effect of welding processes on ferrite content, microstructure and mechanical properties of super duplex stainless steel 2507 welds, Mater. Test., 2023, 65(12): 1836–1844

[7] Song, Q., Wang, H., Wang, W., Han, Z, Qian, Y., Wan, J., et al., Optimization of mechanical and surface properties of friction stir welded dissimilar joint of 2507 SDSS and 317L ASS by controlling process parameters, J. Mater. Res. Technol., 2024, 29: 416–426

[8] Gupta, A., Kumar, A., Baskaran, T., Arya, S.B., Khatirkar, R.K., Effect of heat input on microstructure and corrosion behavior of duplex stainless steel shielded metal arc welds. Trans. Indian. Inst. Met., 2018, 71(7): 1595–1606

[9] Lange, A., Influence of flame straightening on the properties of welded joints made of X2CrNi22-2 duplex steel, Mater. Sci. Pol., 2021, 39: 446–457

[10] Maurya, A.K., Chhibber, R., Pandey, C., GTAW dissimilar weldment of sDSS 2507 and nickel alloy for

marine applications: microstructure–mechanical integrity, Metall. Mater. Trans. A., 2023, 54(8): 3311–3340

[11] El Sayed Seleman, M.M., Alateyah, A.I., Mahmoud, E.A.E., Elsoeudy, R.I., Ahmed, M.M.Z., Hafez, K.M., et al., Friction stir welding of 2507 super-duplex stainless steel: feasibility of butt joint groove filling at different process parameters, Adv. Mater. Process., 2024, 10(4): 40–64

[12] Kumar, S., Yogesh, K., Vimal, K.E.K., Microstructural and corrosion behavior of thin sheet of stainless steel-grade super duplex 2507 by gas tungsten arc welding, SAE Int. J. Mater. Manuf., 2024, 17(2): 9

[13] Cojocaru, E.M., Raducanu, D., Vintilam, A.N., Alturaihi, S.S, Serban, N., Berbecaru, A.C., et al., Influence of ageing treatment on microstructural and mechanical properties of a solution treated UNS S32750/EN 1.4410/F53 Super Duplex Stainless Steel (SDSS) alloy, J. Mater. Res. Technol., 2020, 9(4): 8592–8605

[14] Brum Walter, N.M., Braga Lemos, G.V., Kieckow, G.S., Buzzatti, D.T., Buzzatti, J.T., Mattei, F., et al., Investigating microstructure, mechanical properties, and pitting corrosion resistance of UNS S32760 super duplex stainless steel after linear friction welding, J. Mater. Res. Technol., 2024, 31: 1637–1643

[15] Maurya, A.K., Kumar, N., Pandey, C., Chhibber, R., Structure–property relationship assessment of dissimilar gas tungsten arc welded joint of pipeline steel and super duplex stainless steel for marine applications, Arch. Civ. Mech. Eng., 2024, 24(3): 164

[16] Giorjão, R.A.R., Pereira, V.F., Terada, M., da Fonseca, E.B., Marinho, R.R., Garcia, D.M., et al., Microstructure and mechanical properties of friction stir welded 8mm pipe SAF 2507 super duplex stainless steel, J. Mater. Res. Technol., 2019, 8(1): 243–249

[17] Maurya, A.K., Patnaik, A., Pandey, S.M., Chhibber, R., Pandey, C., Tribological performance of gas tungsten arc welded dissimilar joints of sDSS 2507/N50 steel, J. Mater. Eng. Perform., 2023, 33: 10280–10294

[18] Abbasi, M., Tahaei, A., Vanani, B.B., Post-weld heat treatment and Nitrogen application in welding of super duplex stainless steels, In: Advances in Manufacturing for Aerospace Alloys, S. Gürgen, Springer Nature Switzerland, Cham, 2024, pp. 117–134

[19] Silva, D., Barbosa, E., Pardal, J.M., Barbosa, C., Tavares, S.S.M., Microstructural characterization of aged welded joints of a UNS S32750 superduplex stainless steel metallogr, Microstruct. Anal., 2024, 13: 570–581

[20] Fande, A., Kalbande, V., Kavishwar, S., Tandon, V., Dhunde, A., Enhancing microstructure and mechanical properties of dissimilar TIG welded duplex 2205 and Ni-based inconel 718 superalloy through post weld heat treatment, Eng. Res. Express., 2024, 6(2): 025539

[21] Acuna, A., Riffel, K.C., Ramirez, A., Effect of sigma phase on CVN impact toughness in HDSS weld metal, Mater. Sci. Eng. A., 2024, 912: 146948

[22] Kumar, S., Vimal, K.E.K., Numerical and experimental studies of thin super duplex stainless steel GTAW joints, Int. J. Mater. Eng. Innov., 2024, 15(2): 157–171

[23] Kumar, N., Kumar, P., Investigation on microstructural and mechanical integrity of GTAW dissimilar welded joint of IN 718/ASS 304L using Ni-based filler IN 625 using EBSD and DHD techniques, Int. J. Press. Vessel. Pip.; 2024, 209: 105213

[24] Abbasi, M., Vanani, B.B., Tahaei, A., Garagnani, G.L., Influence of Ni and PWHT on microstructure evolution and mechanical properties of GTA-welded duplex stainless steel and super duplex stainless steel joints: A comparative investigation, Proc. Inst. Mech. Eng. Pt. L J. Mater. Des. Appl., 2024, 238(10): 14644207241236743

[25] Tabrizi, T.R, Sabzi, M., Anijdan, S.M., Eivani, A.R., Park, N., Jafarian, H.R., Comparing the effect of continuous and pulsed current in the GTAW process of AISI 316L stainless steel welded joint: microstructural evolution, phase equilibrium, mechanical properties and fracture mode, J. Mater. Res. Technol., 2021, 15: 199–212

[26] Ramkumar, K.D., Mishra, D., Ganesh Raj, B., Vignesh, M.K., Thiruvengatam, G., Sudharshan, S.P., et al., Effect of optimal weld parameters in the microstructure and mechanical properties of autogeneous gas tungsten arc weldments of super-duplex stainless steel UNS S32750, Mater. Des., 2015, 66: 356–365

[27] Vahman, M., Shamanian, M., Golozar, M.A., Jalali, A., Sarmadi, M.A., Kangazian, J., The effect of welding heat input on the structure–property relationship of a new grade super duplex stainless steel, Steel Res. Int., 2020, 91(1): 1900347

[28] Srinivasan, S., Atrens, A., Effect of pulse gas tungsten arc welding on the metallurgical characteristics & microstructural evolution in AZ31B magnesium alloy welds, J. Mater. Res. Technol., 2024, 29: 295412–295424

[29] Shin, Y.T., Shin, H.S., Lee, H.W., Effects of heat input on pitting corrosion in super duplex stainless steel weld metals, Met. Mater. Int., 2012, 18(6): 1037–1040

[30] Kordatos, J.D., Fourlaris, G., Papadimitriou, G., The effect of cooling rate on the mechanical and

corrosion properties of SAF 2205 (UNS 31803) duplex stainless steel welds, Scr. Mater., 2001, 44(3): 401–408

[31] Tavares, S.S.M., Pardal, J.M., Lima, L.D., Bastos, I.N., Nascimento, A.M., Souzam, J.A., Characterization of microstructure, chemical composition, corrosion resistance and toughness of a multipass weld joint of superduplex stainless steel UNS S32750, Mater. Charact., 2007, 58(7): 610–616

[32] Yousefieh, M., Shamanian, M., Saatchi, A., Optimization of the pulsed current gas tungsten arc welding (PCGTAW) parameters for corrosion resistance of super duplex stainless steel (UNS S32760) welds using the Taguchi method, J. Alloy. Compd., 2011, 509(3): 782–788

[33] Srirangan, A.K., Paulraj, S., Multi-response optimization of process parameters for TIG welding of Incoloy 800HT by Taguchi grey relational analysis, Eng. Sci. Technol. Int. J., 2016, 19(2): 811–817

[34] Magudeeswaran, G., Nair, S.R., Sundar, L., Harikannan, N., Optimization of process parameters of the activated tungsten inert gas welding for aspect ratio of UNS S32205 duplex stainless steel welds, Def. Technol., 2014, 10(3): 251–260

[35] Madugula, N.S., Kumar, Y., Vimal, K.E.K., Kumar, S., Benchmarking the quality improvement strategies of wire arc additive manufacturing process using fuzzy QFD approach, Rapid Prototyp. J., 2024, 30(5): 876–884

[36] Kumar, S., Vimal, K.E.K., Karpagaraj, A., Mechanical characterization and simulation of PCGTAW welded thin sheet of SDSS material, Mater. Today: Proc., 2022, 60: 452–458

[37] Kumar, S., Madugula, N.S., Kumar, R., Kumar, N., Giri, J., Kanan, M., An extensive analysis of GTAW process and its influence on the microstructure and mechanical properties of SDSS 2507, J. Mater. Res. Technol., 2024, 33: 8675–8686

[38] Sordetti, F., Palombi, A., Varone, A., Picco, N., Magnan, M., Marin, E., et al., Experimental review and accuracy of etchants used for phase analysis of SAF2507 Super Duplex Stainless Steel, J. Mater. Res. Technol., 2024, 32: 3842–3856

[39] Çetinarslan, C.S., Sahin, M., Karaman Genç, S., Sevil, C., Mechanical and metallurgical properties of ion-nitrided austenitic-stainless steel welds, Mater. Sci. Pol., 2012, 30: 303–312

[40] Yelamasetti, B.G., Vardhan, V., Optimization of GTAW parameters for the development of dissimilar AA5052 and AA6061 joints, Mater. Today Proc., 2021, 47: 4350–4356

[41] Kumar, S., Vimal, K.E.K., Khan, M.A., Kumar, Y., A hybrid learning approach for modelling the fabrication of super duplex stainless steel thin joints using GTAW process. Int. J. Interact. Des. Manuf., 2024, 18(5): 3001–3014